Geostrophic Eddies Spread Near-Inertial Wave Energy to High Frequencies

WENJING DONG,[a] OLIVER BÜHLER,[a] AND K. SHAFER SMITH[a]

[a] *Courant Institute of Mathematical Sciences, New York University, New York, New York*

(Manuscript received 12 July 2022, in final form 14 February 2023, accepted 21 February 2023)

ABSTRACT: The generation of broadband wave energy frequency spectra from narrowband wave forcing in geophysical flows remains a conundrum. In contrast to the long-standing view that nonlinear wave–wave interactions drive the spreading of wave energy in frequency space, recent work suggests that Doppler-shifting by geostrophic flows may be the primary agent. We investigate this possibility by ray tracing a large number of inertia–gravity wave packets through three-dimensional, geostrophically turbulent flows generated either by a quasigeostrophic (QG) simulation or by synthetic random processes. We find that, in all cases investigated, a broadband quasi-stationary inertia–gravity wave frequency spectrum forms, irrespective of the initial frequencies and wave vectors of the packets. The frequency spectrum is well represented by a power law. A possible theoretical explanation relies on the analogy between the kinematic stretching of passive tracer gradients and the refraction of wave vectors. Consistent with this hypothesis, the spectrum of eigenvalues of the background flow velocity gradients predicts a frequency spectrum that is nearly identical to that found by integration of the ray tracing equations.

KEYWORDS: Ocean; Dynamics; Internal waves; Oceanic waves

1. Introduction

The breaking of inertia–gravity waves at small spatial–temporal scales is a major source of diapycnal mixing (Alford et al. 2016; MacKinnon et al. 2017; Whalen et al. 2020) which regulates meridional overturning circulation, ocean heat, and carbon uptake. Inertia–gravity waves are mainly generated by wind forcing, interaction between large-scale flows and topography, and adjustment of unbalanced flows (Shakespeare and Taylor 2014). Their wavelengths and intrinsic frequencies—which lie between the Coriolis parameter f and the stratification frequency N—are modulated by wave–wave interactions, as well as by interactions with large-scale flows as they propagate through the ocean's interior. To a remarkable degree, the observed spectral energy density of oceanic inertia–gravity waves is well described by the Garrett–Munk (hereafter GM) spectrum (Garrett and Munk 1972, 1975; Polzin and Lvov 2011).

The prevailing view has long been that the observed spectrum of inertia–gravity wave energy is independent of the large-scale, slowly varying balanced flow. In this view, wave action is injected both at low frequency by the storm-generated excitation of near-inertial energy, and at multiple frequencies by tides, then spread among scales and frequencies by nonlinear wave–wave interactions (e.g., Sugiyama et al. 2009). Recently, however, multiple lines of research have suggested that geostrophic flows do not just contribute to the spreading wave energy, but may play the dominant role. A key example comes from the work of Barkan et al. (2017). Using carefully designed high-resolution numerical simulations, they show that when near-inertial waves are generated in the absence of geostrophic flows, wave energy remains localized in the near-inertial band; by contrast, when near-inertial waves are generated in the presence of a well-developed mesoscale eddy field, wave energy readily spreads to higher frequencies, forming a stable energy spectrum consistent with GM. Thomas and Arun (2020) demonstrate a similar result using a two-mode Boussinesq model that effectively captures the interaction of quasigeostrophic baroclinic turbulence and an inertia–gravity wave mode.

Hints of the influence of geostrophic flows on waves are found in recent theoretical work. In both shallow water (Ward and Dewar 2010; Savva and Vanneste 2018) and Boussinesq (Lelong and Riley 1991; Savva et al. 2021) systems, it is found that when wave energy is injected at near-inertial frequencies, geostrophic flows are very effective at spreading wave energy among wavenumbers of the same frequency. For the Boussinesq case, Kafiabad et al. (2019) recasts the "induced diffusion" regime of McComas and Bretherton (1977) to a system in which the large-scale slow wave field is replaced by a balanced eddy field that obeys QG scaling. Employing multiscale analysis under the assumptions that the large-scale velocity is independent of time (an extreme limit of a slowly varying flow) and is weaker than the intrinsic group velocity of the waves (i.e., the "weak refraction" approximation), they give a rigorous derivation of a diffusivity that describes the spreading of inertia–gravity wave action density along constant frequency surfaces in wave vector space. They further deduce that there exists a stationary energy spectrum which is a function of wavenumber modulus $|\mathbf{k}|$, and corroborated their findings using direct numerical simulations of the Boussinesq equations.

In rotating shallow water (RSW), surfaces of constant frequency in wave-vector space are rings in which all wavenumbers have the same modulus. Applying the theoretical analysis of Kafiabad et al. (2019) to the RSW system, Dong et al. (2020) showed that while steady geostrophic flows mix wave energy primarily around the ring, *unsteady* geostrophic flows readily spread inertia–gravity wave energy off the ring

Corresponding author: Oliver Bühler, ob8@nyu.edu

DOI: 10.1175/JPO-D-22-0153.1

to higher frequencies. These results were supported by ray tracing simulations.

In the present study we ask, how might geostrophic flows—steady or unsteady—spread wave energy off the constant-frequency cone in the Boussinesq system? A possibility is suggested by the "wave capture" theory of Bühler and McIntyre (2005). Noticing that the equation for the advection of tracer gradients by a background flow is isomorphic to that for the refraction of wave vectors in the ray tracing approach, Bühler and McIntyre (2005) show that wave vectors will be stretched to align with the aspect ratio of the background flow. The implied change of the ratio between vertical and horizontal wavenumbers then implies, through the Boussinesq inertia–gravity wave dispersion relation, that wave frequencies will also change. Notably, this effect applies even to steady background flows, so unsteadiness is not essential.

Here we investigate this possibility numerically, solving the ray tracing equations for wave packets traveling through both a geostrophically turbulent QG flow, and a family of synthetic background flows. We show that wave energy that starts at a single low frequency readily spreads, forming a remarkably robust power law energy spectrum between the Coriolis parameter f and the buoyancy frequency N. Notably, in contrast to our RSW study—and as expected from the wave capture theory—we find this spectrum emerges for both steady and unsteady background flows.

Despite the robust emergence of this power law spectrum in our simulations, it is important to note at the outset some limitations of our simplistic setup. For example, the functioning of the wave capture effect requires a three-dimensional balanced mean flow, hence the effect is absent if the mean flow is barotropic, as then the wave dynamics resembles that of shallow water waves (e.g., Rocha et al. 2018). Also, our mean flows are symmetric with respect to cyclonic and anticyclonic vorticity, which limits their nonlinear validity and in particular cannot address features such as frontogenesis that are known to modify the wave dynamics significantly (e.g., Thomas 2012). These remain topics for future research.

The plan of the paper is as follows: the ray tracing equations and details of the background flows and initial conditions are presented in section 2. The results of an initial ray tracing simulation through a simulated QG flow snapshot, as well as a synthetic flow constructed from the simulated flow, are discussed in section 3. Results for steady and unsteady synthetic turbulent flows are given in sections 4 and 5, a stochastic strain–shear model is provided in section 6, and comparison with a previous study is discussed in section 7. Conclusions and comments are provided in section 8, and the appendix provides the numerical details of our ray tracing simulations.

2. Ray tracing simulations

We study the linear evolution of wave packets with position $\mathbf{x}(t) = (x, y, z)$ and wavenumber vector $\mathbf{k}(t) = (k, l, m)$ in a slowly varying background flow $\mathbf{U}$ by solving the standard ray tracing equations:

$$\frac{d\mathbf{x}}{dt} = \mathbf{U} + \nabla_{\mathbf{k}}\omega(\mathbf{k}), \qquad \frac{d\mathbf{k}}{dt} = -(\nabla_{\mathbf{x}}\mathbf{U})\cdot\mathbf{k}. \tag{1}$$

Here $\nabla_{\mathbf{k}}$ and $\nabla_{\mathbf{x}}$ are gradients with respect to $\mathbf{k}$ and $\mathbf{x}$, respectively, the background flow $\mathbf{U}$ is induced by a geostrophic streamfunction ψ via $\mathbf{U} = (U, V, W) = (-\psi_y, \psi_x, 0)$ and

$$\omega(\mathbf{k}) = \sqrt{\frac{N^2(k^2 + l^2) + f^2m^2}{k^2 + l^2 + m^2}} \tag{2}$$

is the intrinsic frequency of inertia–gravity waves. The Doppler-shifted absolute frequency is $\omega_a = \omega + \mathbf{U}\cdot\mathbf{k}$. Both the Coriolis parameter f and the buoyancy frequency N are constant. We restrict to steady background flows $\mathbf{U}$ for most of the paper, but unsteady flows are eventually considered in section 5.

The impact of the mean flow on a wave packet is measured by the nondimensional parameter

$$\varepsilon = \frac{\sqrt{\langle|\mathbf{U}^2|\rangle}}{|\mathbf{c}|}, \tag{3}$$

where $\mathbf{c} = \nabla_{\mathbf{k}}\omega = (c_x, c_y, c_z)$ is the intrinsic group velocity and angle brackets represent averaging over the computational domain (e.g., Kafiabad et al. 2019; Savva et al. 2021). Intuitively, when $\varepsilon \ll 1$ the wave packet path will deviate little from a straight line, whereas for larger values of ε the refraction and Doppler shifting by the mean flow become significant. All our experiments satisfy $\varepsilon \ll 1$ at the initial time.

Numerical details of our ray tracing simulations are provided in the appendix.

a. *Choice of background flows*

The three-dimensional flow domain $[0, L] \times [0, L] \times [0, -H]$ is doubly periodic in the horizontal directions and bounded in the vertical by rigid walls, where the buoyancy disturbance vanishes. The horizontal deformation length $L_d = 1/k_d$ is based on the horizontal wavenumber $k_d = \pi f/(NH)$ of the first baroclinic mode in this domain. Broadly speaking, the mean flows will scale with L_d in the horizontal and with fL_d/N in the vertical.

We first simulate wave packets for a mean flow taken from a single snapshot of a forced-dissipative QG turbulence simulation (details provided in section 3). Of course, this implies that the mean flow is steady. Then we repeat the experiment with a steady synthetic flow constructed from the QG snapshot by randomizing the phases of its Fourier components. Somewhat surprisingly, this led to basically identical results for the wave packet statistics, and based on this finding subsequent experiments are all done with Gaussian random flows, for which we can precisely specify the statistical properties.

Notably, the parameter ε can be reduced by lowering the amplitude of either $|\mathbf{U}|$ or $|\mathbf{k}|$, the latter because $\mathbf{c}(\mathbf{k})$ is inversely proportional to $|\mathbf{k}|$ for internal waves. Actually, for *steady* flows $\mathbf{U}(\mathbf{x})$ these two approaches are equivalent as far as the ray tracing system (1) is concerned. This can be seen by rescaling $(\mathbf{U}, \mathbf{k}, t) \to (a\mathbf{U}, b\mathbf{k}, t/a)$ with two positive constants (a, b), which modifies (1) by multiplying the group velocity term by $1/(ab)$. [This uses that $\omega(b\mathbf{k}) = \omega(\mathbf{k})$ in (2).] Similarly, ε is multiplied by a factor (ab), so both the ray tracing

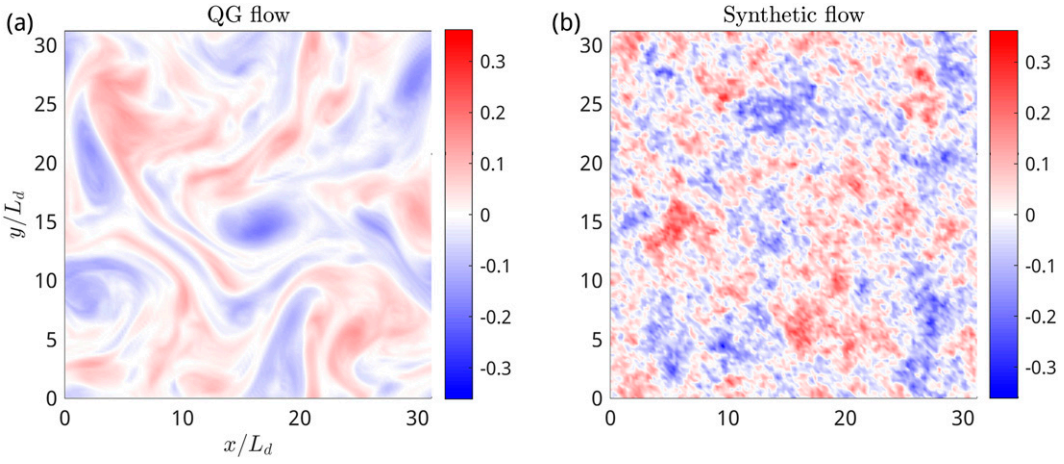

FIG. 1. Normalized vorticity ζ/f at $z = -H/2$ for a QG flow and a synthetic flow with randomized phases. The flows look markedly different but lead to near-identical ray tracing results.

equations as well as ε are only sensitive to the product (ab). For simplicity, we keep $b = 1$ and vary ε exclusively by adjusting the magnitude of the velocity field $\mathbf{U}$. If the Rossby number $\mathrm{Ro} = \sqrt{\langle\zeta^2\rangle}/f$, where $\zeta = V_x - U_y$ is the vorticity, then $\varepsilon \propto \mathrm{Ro}$ if the spatial structure of the mean flow is unchanged. Thus we control the initial ε by varying the Rossby number of the background flow.

b. *Wave packet initial conditions*

Each wave packet is characterized by its initial wave vector (k_0, l_0, m_0) and initial location (x_0, y_0, z_0). To satisfy the WKB approximation, we require $\sqrt{k_0^2 + l_0^2} \gg k_d$ and $|m_0| \gg Nk_d/f$. Specifically, we let $(k_0, l_0) = 10k_d(\cos\theta, \sin\theta)$, where θ is a random variable with uniform distribution on $[0, 2\pi]$. All wave packets in a given experiment have the same initial intrinsic frequency ω_0 and then the vertical wavenumber is $m_0 = \pm\sqrt{(k_0^2 + l_0^2)(N^2 - \omega_0^2)/(\omega_0^2 - f^2)}$, with a randomly chosen sign corresponding to upward or downward propagating packets. There is no restriction for (x_0, y_0, z_0), so we initialize wave packets with uniformly random locations in the domain $[0, L] \times [0, L] \times [0, -H]$.

We chose $\omega_0/f = (2, 4, 5)$ in our different experiments. To illustrate the initial wave packet speeds in these experiments with some round numbers let us consider $N/f = 100$ and $f = 10^{-4}\ \mathrm{s}^{-1}$. Then the horizontal group velocity would be about $(2, 5, 6)\ \mathrm{m\ s}^{-1}$ and the vertical group velocity would be about $(3, 18, 30)\ \mathrm{cm\ s}^{-1}$. This corresponds to a travel distance per day of 200–500 km in the horizontal and 3–30 km in the vertical.

3. Emergence of a stationary frequency spectrum

In this section, we present ray tracing results for a QG flow snapshot and for a synthetic steady flow constructed from it by scrambling the phases of the Fourier modes. For both background flows, $\mathrm{Ro} = 0.1$ and $N/f = 100$, and the results are averaged over 5000 wave packets initialized with intrinsic frequency $\omega_0 = 2f$.

The QG streamfunction $\psi(x, y, z)$ is taken from a standard pseudospectral simulation of forced-dissipated geostrophic turbulence on a horizontally periodic and vertically bounded domain. The domain length and width are $L = 10\pi L_d$, and the resolution is $n_x = n_y = 512$, with $n_z = 100$ equally spaced levels. The flow is forced by a first-baroclinic-mode mean flow, dissipated by quadratic bottom drag, and the Coriolis gradient $\beta = 0$. The buoyancy disturbance is zero at the top and bottom boundaries, and therefore $\partial\psi/\partial z = 0$ there.

The flow used in the ray tracing simulations is subsampled to a horizontal grid size $n_x = n_y = 128$ and interpolated to a vertical grid size $n_z = 100$. Wave packets are reflected when they hit the vertical boundaries by reversing the sign of the vertical wavenumber m. A snapshot of the vertical vorticity during steady state at $z = -H/2$ is shown in Fig. 1a.

We construct a synthetic streamfunction ψ_r as follows. First, the gridded QG streamfunction ψ is rewritten as a (truncated) sum of vertical modes via

$$\psi(x, y, z) = \sum_{n=0}^{20} \psi_n(x, y)\cos\left(\frac{n\pi}{H}z\right) = \sum_{n=0}^{20}\sum_{q_x}\sum_{q_y} \hat{\psi}_n(q_x, q_y)\exp[i(q_x x + q_y y)]\cos\left(\frac{n\pi}{H}z\right). \tag{4}$$

Here $\hat{()}$ denotes the two-dimensional Fourier coefficients in the horizontal domain $[0, L] \times [0, L]$ and, following the notation of Dong et al. (2020), (q_x, q_y) denotes the horizontal wavenumber vector of the mean flow (the unusual symbol is used to distinguish the wavenumbers of the mean flow from those of the waves). Then, the synthetic streamfunction ψ_r is constructed by randomizing the phase of the horizontal Fourier components of $\psi_n(x, y)$, i.e.,

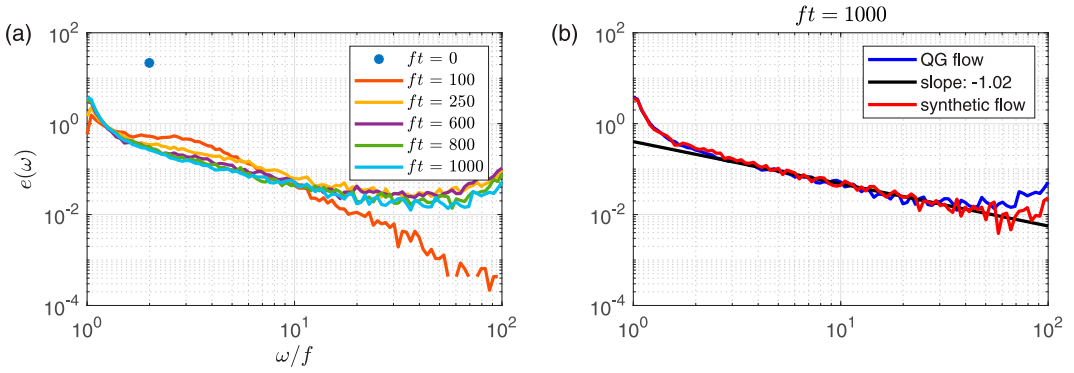

FIG. 2. (a) Evolution of energy spectrum of wave packets in the QG flow of Ro = 0.1. (b) Energy spectra for the QG flow and the synthetic flow of Ro = 0.1. The energy spectrum of the QG flow for $\omega \in [2f, 40f]$ is fitted by a power law with slope −1.02 in this plot.

$$\psi_r = \sum_{n=0}^{20} \sum_{q_x} \sum_{q_y} |\hat{\psi}_n(q_x, q_y)| \exp[i\theta(q_x, q_y, n)] \times \exp[i(q_x x + q_y y)] \cos\left(\frac{n\pi}{H} z\right). \quad (5)$$

The phase $\theta(q_x, q_y, n)$ for each mode is chosen randomly subject only to the reality condition $\theta(q_x, q_y, n) = -\theta(-q_x, -q_y, n)$. This procedure preserves the amplitude of each mode and therefore also rms values such as Ro = 0.1. Figure 1 shows the vorticity at $z = -H/2$ for the two flows, which are of course markedly different (e.g., Armi and Flament 1985). Nonetheless, the ray tracing results for both flows turned out to be nearly identical. There is no obvious explanation for this near-identical behavior, but this of course simplifies our simulation task.

a. The energy spectrum for intrinsic frequency

For steady flows the absolute frequency is conserved along rays by (1), i.e., $d\omega_a/dt = 0$. We use this conservation law as a criterion for measuring the accuracy of the numerical results, e.g., in the present section the maximum error of the absolute frequency relative to ω_0 is less than 10% for both the QG flow and the synthetic flow.

Unlike absolute frequency, there is no constraint that prevents intrinsic frequency from drifting. This can be seen from the evolving distribution of wave packets in frequency space. We construct an energy spectrum $e(\omega)$ of wave packets as a function of frequency by assuming that each wave packet carries the same amount of wave action, which mean that $e(\omega)$ is the product of the intrinsic frequency and the probability density function of the wave packets as a function of frequency. Figure 2a shows the time evolution of the spectrum for the QG flow, starting with a single peak at $\omega = 2f$ at $t = 0$. From there the spectrum spreads through the entire available frequency band and gradually evolves to a seemingly stationary spectrum. The initial spreading across the frequency band is quite quick (e.g., $ft \approx 10$ corresponds to one day at midlatitudes, so this occurs in the span of a couple of weeks) while convergence toward the stationary state takes longer (about a couple of months). Very similar results were obtained for the synthetic flow.

We then ran the simulations for a very long time to check that the emerging spectra were indeed stationary and the results for both flows are compared in Fig. 2b, which shows that the stationary spectra in the QG flow and synthetic flow agree for most frequency values, with discrepancies confined to the ends of the frequency band. The spectrum between $2f$ and $40f$ can be fitted quite well by a power law $e(\omega) \propto \omega^{-1}$.

Of course, the emergence of a stationary frequency spectrum for the internal waves does not imply a stationary wavenumber spectrum. Indeed, the wavenumber magnitude along rays grows on average, and no stationary wavenumber regime can be reached unless forcing and dissipation terms were to be added to the dynamics.

b. Eigenvector theory for the frequency spectrum

We use some elements of the wave capture theory of Bühler and McIntyre (2005) to provide an approximate theory for the observed frequency spectrum. Wave capture theory is based on the (partial) analogy between the evolution of the wavenumber vector $\mathbf{k}(t)$ and of the gradient of a passively advected scalar, which suggests the possibility of exponential growth of $\mathbf{k}(t)$ along three-dimensional eigenvectors of the matrix $-\nabla_x \mathbf{U}$. This can be made precise if one ignores the time evolution of $\nabla_x \mathbf{U}$ along the ray, as then the ODE for $\mathbf{k}(t)$ in (1) has constant coefficients and is readily solved [see details in Bühler and McIntyre (2005), for example].

Specifically, for $\mathbf{U} = (U, V, 0)$ with $U_x + V_y = 0$ the eigenvalues of $-\nabla_x \mathbf{U}$ are $\lambda = 0$ and $\lambda = \pm\sqrt{D}$ where

$$D = U_x^2 + V_x U_y \quad (6)$$

is the Okubo–Weiss parameter. If $D < 0$ then the nonzero eigenvalues are imaginary and there is no exponential growth. But if $D > 0$ then there exists a positive eigenvalue and the corresponding eigenvector will grow as $\exp(+\sqrt{D}t)$, which implies that $\mathbf{k}(t)$ will eventually become aligned with this eigenvector for almost all initial conditions $\mathbf{k}(0)$. Crucially, the direction of $\mathbf{k}(t)$ determines the intrinsic frequency ω, which implies that ω will tend toward a limiting value determined by the direction of this eigenvector. This provides a simple

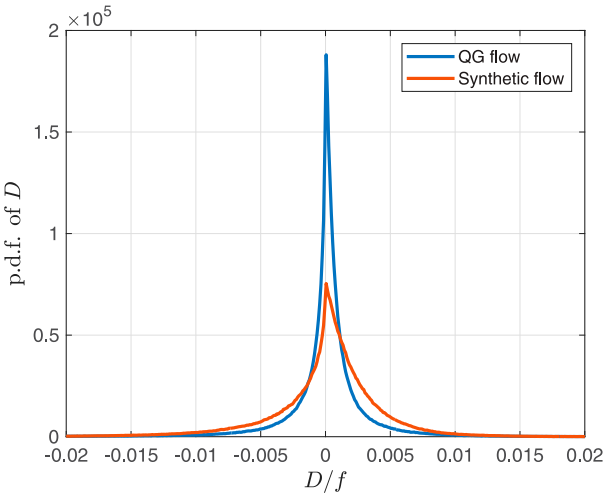

FIG. 3. Histograms of D for the QG and synthetic flows with Rossby number Ro = 0.1. For both flows the probability of $D > 0$ is about 58%. For the QG flow, $\mathbb{E}\left[\sqrt{D}|D>0\right] = 0.033\sqrt{f}$. For the synthetic flow, $\mathbb{E}\left[\sqrt{D}|D>0\right] = 0.044\sqrt{f}$.

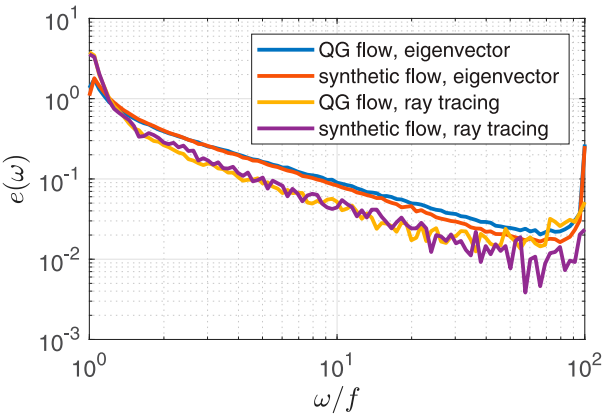

FIG. 4. Frequency spectra obtained by using the growing eigenvector method compared to numerical results from ray tracing simulations.

approximate theory for a stationary frequency spectrum based solely on the statistics of the eigenvalues and eigenvectors of the random field $\nabla_x \mathbf{U}$.

Figure 3 shows the histograms of D for the QG and synthetic flows, from which one can estimate the overall probability of $D > 0$ as well as the conditional mean of $+\sqrt{D}$ given $D > 0$. It turns out that the probability of $D > 0$ is about 58% in both flows, so $D > 0$ is more likely than $D < 0$. For the QG flow this is compatible with the intuitive idea of isolated strong vortices surrounded by large areas of straining flow, but for the disorganized synthetic flow this is purely an empirical result, and we were surprised that this probability was essentially the same. In particular, that the probability of $D > 0$ is about 58% in both flows suggests a fairly universal validity of this percentage, which would be of interest to explore in realistic ocean flows. On the other hand, the two histograms for D in Fig. 3 are qualitatively different, which affects more detailed flow statistics. For example, the QG histogram is narrower than the synthetic flow histogram. Hence, the mean value of $+\sqrt{D}$ conditioned on $D \geq 0$ is slightly higher in the synthetic flow, which suggests that eigenvectors of positive eigenvalues may grow slightly faster for the synthetic background flow. This links to a direction of future research, which was pointed out to us by a referee, namely, to investigate how different ways of randomizing the flow affect the distribution of D and subsequently the time scale for establishing a stationary spectrum. From our limited experience so far it seems that the autocorrelation function of the velocity field (which is the Fourier transform of its power spectrum and hence invariant under phase scrambling) is the rate-limiting factor for the emergence of the stationary spectrum. This requires further investigation.

Now, we construct a predicted energy spectrum using the gridded $-\nabla_{\mathbf{x}}\mathbf{U}$ field by the following algorithm. For each grid point, we compute D, and ignore the point if $D < 0$. If $D > 0$ we compute the eigenvector (a wavevector $\mathbf{k}$) associated with $\lambda = +\sqrt{D}$ and use this vector in the dispersion relation (2) to find the corresponding frequency ω. This produces a probability distribution of ω, and we assume that the wave action spectrum is proportional to this ω distribution, with a suitable normalization constant such that the total wave action is conserved. Finally, the action spectrum is converted into an energy spectrum by multiplying it with ω to produce $e(\omega)$. Notably, this theoretical spectrum conserves total wave action but not total wave energy, which can be modified via interactions with the mean flow. Also, the prediction for the theoretical spectrum is independent of the overall amplitude of the mean flow, which affects only the magnitude of D but not its sign, or the direction of the associated eigenvectors.

Figure 4 compares the theoretical and observed spectra obtained for the QG and synthetic flows, which shows a good fit over a broad frequency range, although the amplitude of the theoretical spectra is higher than the observed amplitude for most frequency values. We show in section 5 that the fit between the theoretical and numerical spectra is significantly improved if the mean flow is allowed to be time dependent.

4. Experiments with triply periodic Charney turbulent flows

In the previous section, we found that after sufficient time moving through a balanced eddy field, wave packets initialized at the same frequency form a stationary energy spectrum, and that the spectrum formed by a simulated QG flow is nearly identical to that formed by a synthetic flow with similar statistical properties. Thus, it suffices to use synthetic flows to investigate the questions that we are interested in. In this section, we use synthetic triply periodic flows constructed to follow the three-dimensional energy spectrum predicted for the forward cascade of potential enstrophy in geostrophic turbulence (Charney 1971)—we term these "Charney turbulent flows"—and show that the stationary wave energy spectrum does not depend on the initial intrinsic frequency ω_0 or the Rossby number Ro.

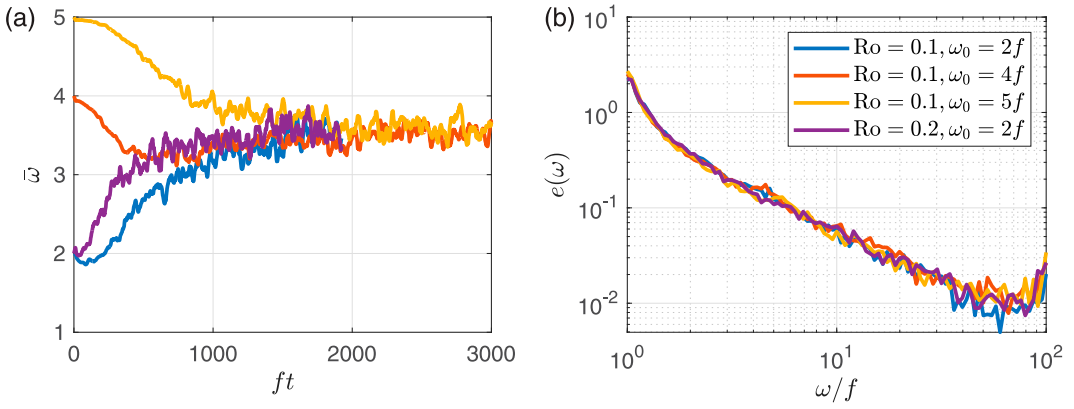

FIG. 5. (a) Evolution of average intrinsic frequency $\overline{\omega}$ for synthetic Charney turbulent flows. (b) Stationary energy spectra for synthetic Charney turbulent flows.

In the forward enstrophy cascade regime of geostrophic turbulence, the energy spectrum depends only on the magnitude of the scaled wavenumber vector $\mathbf{q}_s = (q_x, q_y, q_z f/N)$. For a band-limited random-phase streamfunction this can be realized via

$$\psi = C \sum_{\mathbf{q}_s : Q_1 < q_s < Q_2} \exp[i(q_x x + q_y y + q_z z + \theta)] q_s^{-7/2}, \quad (7)$$

where the constant C is controlled by Ro and θ is a random phase as before. We chose band limits $Q_1 = k_d$ and $Q_2 = 50k_d$ and set $H = Lf/N$ so that the domain size is isotropic in the scaled wavenumber space.

In Fig. 5a, we plot the evolution of the ensemble-averaged frequency $\overline{\omega}$ for different ω_0 and Ro. For Ro = 0.1, $\overline{\omega}$ clearly converges to the same value for different ω_0. For Ro = 0.2, $\overline{\omega}$ seems to converge to the same value. In Fig. 5b, we compare the stationary energy spectra for these runs. The stationary energy spectra match very well. These findings appear to support the validity of our theoretical eigenvector model, which implies both of these results.

The synthetic Charney turbulent flows we used are isotropic in scaled wave vector space, so we expect the energy spectrum not to change in the common frequency range when we vary the ratio N/f. Figure 6 shows that the stationary energy spectra for different N/f indeed agree in the common frequency range as expected. In the same figure, we also plotted the energy spectrum obtained from eigenvector analysis for $N/f = 100$. The energy spectrum from eigenvector analysis has a similar shape to the stationary energy spectra obtained from ray tracing simulations. As we have observed in Fig. 4, the spectrum obtained from eigenvector analysis has higher energy than the stationary energy spectrum obtained from ray tracing simulations for most frequency values. However, it provides a good estimate for the slope of the stationary energy spectra.

5. Unsteady background flows

We extend our setup to include a simple stochastic model for an unsteady background flow. This is achieved by letting the Fourier coefficients of ψ evolve in time as independent Ornstein–Uhlenbeck (OU) processes (subject to the reality condition, as usual). This means (7) is replaced by

$$\psi = C \sum_{\mathbf{q}_s : Q_1 < q_s < Q_2} \exp[i(q_x x + q_y y + q_z z)] \frac{a(\mathbf{q}_s, t) + ib(\mathbf{q}_s, t)}{\sqrt{2}} q_s^{-7/2}, \quad (8)$$

where $a(\mathbf{q}_s, t)$ and $b(\mathbf{q}_s, t)$ are independent OU processes governed by

$$da = -\sigma\, dt + \sqrt{2\sigma}\, dW, \qquad db = -\sigma\, dt + \sqrt{2\sigma}\, dW', \quad (9)$$

where dW and dW' are independent normal random variables with mean zero and variance equal to dt. With this choice $a, b \sim \mathcal{N}(0, 1)$ holds for any value of the parameter $\sigma > 0$. This parameter governs the temporal autocorrelation of the Fourier coefficients, i.e., the expected value of $a(t)a(t + \tau)$ with $\tau \geq 0$ is equal to $\exp(-\sigma\tau)$, so $1/\sigma$ can be interpreted as the autocorrelation time scale. Formally, a steady flow is then included as the limit $\sigma \to 0$. To compare with realistic

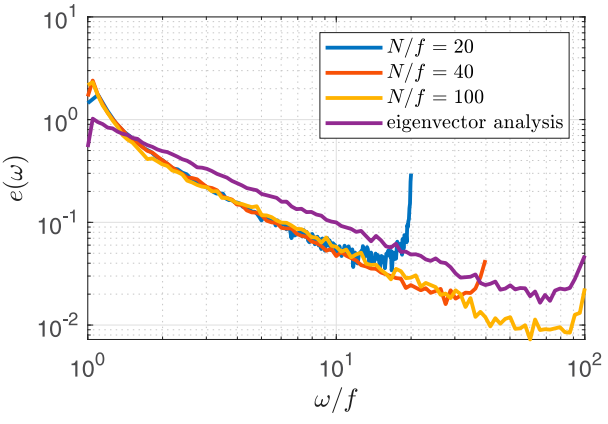

FIG. 6. Stationary energy spectra in synthetic Charney turbulent flows for $N/f = 20, 40, 100$, and the stationary energy spectrum obtained from eigenvector analysis.

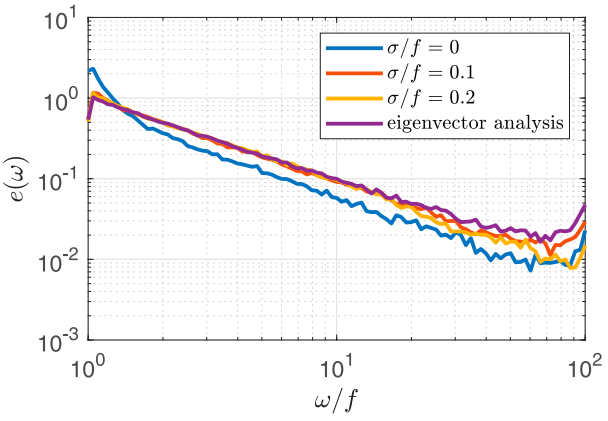

FIG. 7. Stationary energy spectra in unsteady synthetic flows and energy spectrum obtained using eigenvector analysis.

geostrophic flows one should view $1/\sigma$ as proportional to the eddy turnover time, for example. In the present setting a natural choice is to consider σ to be proportional to the Rossby number Ro.

Figure 7 shows the stationary energy spectra for the three values $\sigma/f = 0$, 0.1, 0.2 as well as the theoretical energy spectrum obtained from eigenvector analysis using a snapshot of the velocity field. The spectrum for $\sigma = 0$ is the same as the spectrum found for steady flows before (see Fig. 5b). Surprisingly, the energy spectra for $\sigma/f = 0.1$, 0.2 are nearly identical to each other (but different from the spectrum for $\sigma = 0$) and also agree almost perfectly with the theoretical spectrum. It is unclear exactly why this occurs, but it indicates an improved validity of the eigenvector analysis once the flow is unsteady. Hypothetically, this might be because an evolving mean flow avoids the spatial trapping of some rays within certain flow features, which therefore allows all rays to experience the full statistical properties of $-\nabla_x \mathbf{U}$ on which the eigenvector theory was based. Of course, the OU model for the time evolution that we used here can only be a cartoon of realistic time-dependent ocean flows, for at least two reasons. First, it does not preserve any coherent structures such as long-lived vortices marked by strong potential vorticity values. And second, like QG flow, it does not distinguish between cyclonic and anticyclonic regions.

6. Stochastic strain–shear model for the frequency spectrum

Motivated by the success of the eigenvector theory in section 3b we considered the even simpler stochastic trajectory model of Haynes and Anglade (1997, hereafter HA97), which was originally developed to study passive tracer advection in the atmosphere. The connection between HA97 and ray tracing was discussed qualitatively in Bühler and McIntyre (2005) and it arises because of the aforementioned analogy between the evolution of the wavenumber vector and of the gradient of a passive tracer. In particular, in the present situation both evolve by the wavenumber part of the ray tracing equations (1), i.e.,

$$\frac{d}{dt}\begin{pmatrix} k \\ l \end{pmatrix} = -\begin{pmatrix} U_x & V_x \\ U_y & V_y \end{pmatrix}\begin{pmatrix} k \\ l \end{pmatrix} \quad \text{and} \quad \frac{dm}{dt} = -U_z k - V_z l. \tag{10}$$

Notably, the horizontal components (k, l) evolve independently of the vertical component m, which can be solved for subsequently. In HA97 the time derivative is taken along material trajectories, so there is no group velocity. HA97 proposed a stochastic trajectory model for studying (10), in which the velocity gradient components were approximated by independent Ornstein–Uhlenbeck processes. They also restricted to perfect horizontal straining fields such that $U_x + V_y = 0$ and $V_x = U_y$. (The latter is not possible with a doubly periodic QG flow, where the vertical curl is necessarily nonzero.) Hence two independent processes $a(t) = -U_x = V_y$ and $b(t) = -V_x = -U_y$ were sufficient to model the evolution of (k, l). For this strain-only model the Okubo–Weiss parameter $D = a^2 + b^2$ is always positive so there is always a growing eigenvector with growth rate $\sqrt{D} = \sqrt{a^2 + b^2}$. The vertical shear components (U_z, V_z) were similarly modeled by independent processes, but allowing for different parameters in their distribution compared to the horizontal components.

HA97 showed that these equations can be solved explicitly in certain limits, including the limit of a slowly varying mean flow where (a, b) were effectively constant in time and drawn independently from a normal distribution with mean zero and variance γ_h^2. In this case (k, l) are stretched along the growing eigenvector and eventually the horizontal wavenumber magnitude k_h becomes well approximated by $k_h = A\exp(\sqrt{D}t)$ for some $A > 0$. The long-term evolution of m then depends on the projection of the growing horizontal eigenvector onto the shear (U_z, V_z) such that $\dot{m} = -k_h \tilde{U}_z$, say. This implies that eventually m becomes well approximated by $m = -\left(\tilde{U}_z/\sqrt{D}\right)A\exp(\sqrt{D}t)$ and therefore the aspect ratio converges to $m/k_h = -\tilde{U}_z/\sqrt{D}$. This ratio depends on the independent random variables $(a, b, \tilde{U}_z)$. The random direction of the horizontal eigenvector is independent of the shear and hence $\tilde{U}_z$ is equal in distribution to either U_z or V_z, which in HA97 were modeled as zero-mean normal distributions with variance $\gamma_v^2 \gg \gamma_h^2$. Under these assumptions HA97 demonstrated that the distribution of the random aspect ratio $X = |m|/k_h$ could be found explicitly, yielding the probability density function

$$p_X(x) = \frac{\alpha^2}{(\alpha^2 + x^2)^{3/2}}, \quad \text{where } \alpha = \frac{\gamma_v}{\gamma_h} \gg 1 \tag{11}$$

and α is also equal to the expected value of $X = |m|/k_h$. Again, the mean flow aspect ratio α is imprinted on the wavenumber aspect ratio.

We leverage this result to derive a corresponding probability density function for the frequency via the dispersion relation (2), which establishes a one-to-one link between $\omega \in [f, N]$ and $X \geq 0$ as

$$\omega(X) = \sqrt{\frac{N^2 - f^2}{1 + X^2} + f^2} \quad \text{and} \quad X(\omega) = \sqrt{\frac{N^2 - \omega^2}{\omega^2 - f^2}}. \tag{12}$$

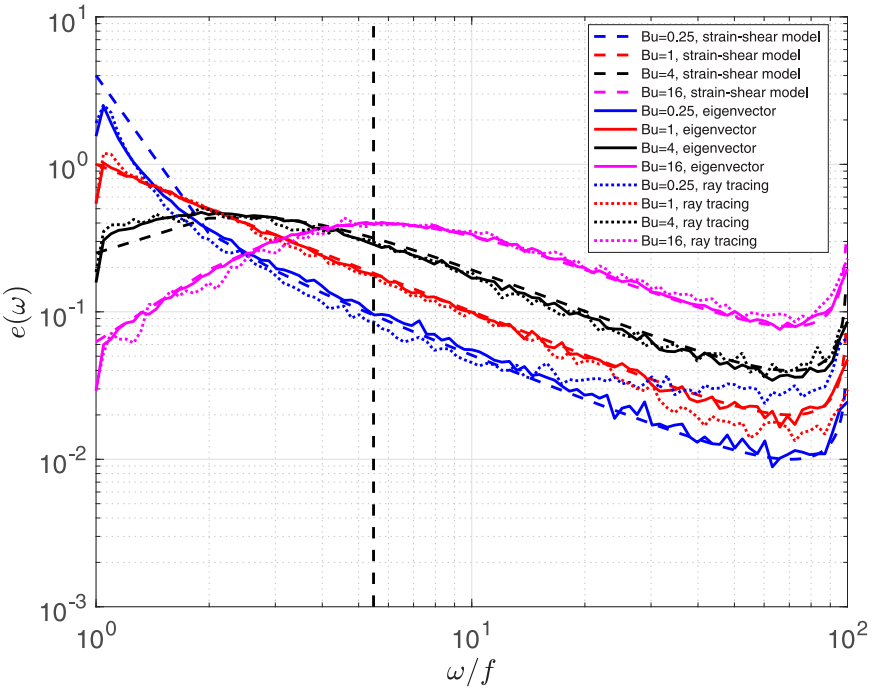

FIG. 8. Energy spectra obtained using three methods: prediction (16) by the strain-shear model (dashed lines); eigenvector analysis (solid lines); ray tracing simulations (dotted lines). The vertical dashed line is $\omega/f = \sqrt{2(\mathrm{Bu}-1)}$ where Bu = 16.

Conservation of probability implies $p(\omega)d\omega = p_X(x)dx$ and hence the probability density function for the frequency is

$$p(\omega) = p_X[x(\omega)]\left|\frac{dx}{d\omega}\right|. \tag{13}$$

Working out the details from (11)–(13) yields

$$p(\omega) = \frac{N^2 - f^2}{\sqrt{N^2-\omega^2}}\frac{\alpha^2\omega}{[N^2 + (\alpha^2-1)\omega^2 - \alpha^2 f^2]^{3/2}}. \tag{14}$$

The interpretation of (14) in the context of our ray tracing experiments is that the distribution of ω over all rays starts with a delta function at the common initial value and subsequently evolves toward this steady distribution. Hence, if we assume that all rays start with the same amount of conserved wave action, then in the long run the wave action spectrum will be proportional to $p(\omega)$ and so the energy spectrum will be proportional to $e(\omega) \propto \omega p(\omega)$. Using this as well as $N^2 \gg f^2$ and $\alpha^2 \gg 1$ we can simplify (14) to

$$e(\omega) = \overline{A}\,\frac{N^2}{\sqrt{N^2-\omega^2}}\frac{\alpha^2\omega^2}{[N^2 + \alpha^2(\omega^2 - f^2)]^{3/2}}, \tag{15}$$

where $\overline{A}$ is the expected value of $e(\omega)/\omega$. This leads to testable predictions of the stochastic strain–shear model.

Model spectrum and Burger number

The model spectrum (15) depends on the mean flow aspect ratio parameter $\alpha \gg 1$, or equivalently on the Burger number $\mathrm{Bu} = N^2/(f^2\alpha^2)$. This can be made explicit by rewriting (15) in terms of Bu as

$$e(\omega) = \overline{A}\,\frac{fN}{\sqrt{N^2-\omega^2}}\frac{\omega^2\sqrt{\mathrm{Bu}}}{[\omega^2 + (\mathrm{Bu}-1)f^2]^{3/2}}. \tag{16}$$

For the Charney regime Bu = 1 this yields

$$e(\omega) = \overline{A}\,\frac{fN}{\sqrt{N^2-\omega^2}\,\omega}, \tag{17}$$

which exhibits a global ω^{-1} power law modified by an integrable singularity as $\omega \to N$. This is consistent with our ray tracing results except that the observed amplification of the spectrum as $\omega \to f$ is missing. However, this amplification is recovered if $\mathrm{Bu} < 1$ as then the denominator has a singularity at $\omega/f = \sqrt{1-\mathrm{Bu}} > 0$.

Surprisingly, for $\mathrm{Bu} > 1$ the model predicts an interior maximum of $e(\omega)$ at $\omega/f \approx \sqrt{2(\mathrm{Bu}-1)}$. This regime could be reached by a mean flow with a strong barotropic component, for example. Such a wave energy maximum is unrelated to the wave sources and entirely due to the interplay of the dispersion relation and the mean flow.

We compare the predicted energy spectrum (16) by the strain-shear model, with stationary energy spectra obtained by ray tracing simulations and spectra obtained by the eigenvector analysis in section 3b. To change Bu, we modify the steam function in (8) by redefining q_s as

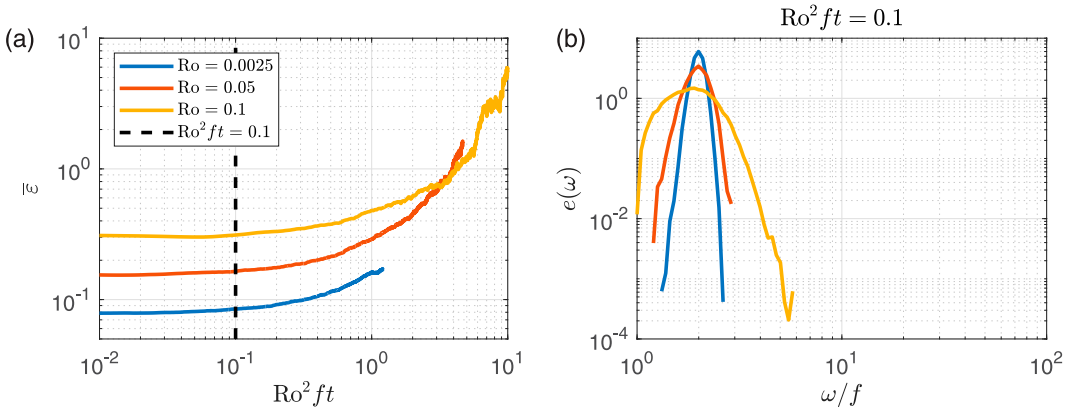

FIG. 9. (a) Evolution of $\overline{\varepsilon}$ for synthetic Charney turbulent flows of different Ro, and (b) energy spectra at $\mathrm{Ro}^2ft = 0.1$. For the initial conditions used for these runs, $\varepsilon_0 = 3.12\mathrm{Ro}$.

$$\mathbf{q}_s = \left(q_x, q_y, \sqrt{\mathrm{Bu}}\frac{f}{N}q_z\right). \tag{18}$$

For those streamfunctions, Ro = 0.1, $\sigma/f = 0.1$.

In Fig. 8, we plot the stationary energy spectra ray tracing simulations, and energy spectra predicted by the eigenvector analysis and the strain-shear model for Bu = 0.25, 1, 4, 16. As we have shown previously, the stationary energy spectra match with the prediction by eigenvector analysis. Moreover, the stationary energy spectra match with the prediction by the strain-shear model very well. For Bu > 1, the energy spectrum is predicted to has a maximum at $\omega/f \approx \sqrt{2(\mathrm{Bu}-1)}$. The figure shows that this is a good estimation for Bu = 16.

7. Relation to wavenumber diffusion theory

Recently, Kafiabad et al. (2019) analyzed the ray tracing equations (1) for internal waves using a multiscale analysis based on weak steady mean flows and found that the dominant dynamics was diffusion of wave action in wavenumber space confined to cones of constant intrinsic frequency ω. This conservation of ω as $\mathbf{k}$ diffuses is obviously completely different from the dynamics we have observed and studied in this paper. Moreover, our stationary spectra were shown to be independent of Rossby number and should therefore be valid also in the limit of weak mean flows that was assumed in their wavenumber diffusion theory, which seems to be a contradiction. In this section, we show that our results are actually consistent with their results, which comes down to a careful consideration of time scales and the range of validity in time of the two theories.

In Kafiabad et al. (2019) a small asymptotic parameter $\varepsilon \ll 1$ measures the weakness of the mean flow compared to the initial group velocity of the wave packets and the frequency-conserving wavenumber diffusion is then established for time intervals such that $\varepsilon^2 t = O(1)$. Consequently, the frequency spreading we observe must occur on a longer time scale than that. In particular, the frequency spreading observed at some fixed $\varepsilon^2 t$ must become weaker as ε decreases. Denote the initial value of ε by ε_0. We tested this by identifying ε_0 with the Rossby number Ro and performing a sequence of runs with decreasing Ro and plotting the results as a function of the slow time Ro^2ft. In these runs f was kept fixed and Ro was varied by changing the amplitude of the mean flow. Using the specific definition of ε in Kafiabad et al. (2019) gives that in these runs initially $\varepsilon_0 = 3.12\mathrm{Ro}$, which means $\varepsilon_0^2 ft$ is about 10 times larger than Ro^2ft.

Figure 9a shows initially $\overline{\varepsilon} = U/|\overline{\mathbf{c}}|$ is less than 1 for all the cases and the weak refraction approximation is valid. However, this parameter grows instead of remaining small. Eventually, the weak refraction approximation breaks down and the multiscale analysis in Kafiabad et al. (2019) no longer holds. Notably, $\overline{\varepsilon}$ starts growing at around $\mathrm{Ro}^2ft = 0.1$, which corresponds to $\varepsilon_0^2 ft \approx 1$. Figure 9b shows the energy spectra at $\mathrm{Ro}^2ft = 0.1$ for the three runs and, consistent with wave diffusion theory, the spread of energy in frequency space becomes weaker as Ro decreases.

We can conclude from this that our results describe the evolution that ensues *after* wave diffusion theory has ceased to be valid, which occurs at a time horizon that depends sensitively on the flow amplitude. Our stationary frequency spectra were independent of this flow amplitude precisely because they were the ultimate end states of an evolution that is only briefly described by wave diffusion theory. In practice, one would have to consider the actual flow amplitudes and details to discern the precise upper limit of Ro^2ft for which wave diffusion is the dominant mechanism; in our examples here $\mathrm{Ro}^2ft \approx 0.1$ seemed to be close to that limit.

8. Discussions

We have conducted large-scale ray tracing simulations of three-dimensional inertia–gravity waves in background flows generated both by direct numerical simulation of the QG equations, and synthetically. Using asymptotic analysis and numerical simulations of the Boussinesq equations, Kafiabad et al. (2019) demonstrate that wave action diffuses on constant frequency surfaces. Our ray tracing simulations show that, on longer time scales than considered by Kafiabad et al. (2019), wave packets do not remain on constant frequency surfaces. Moreover, the intrinsic frequency of inertia–gravity

waves spread, and the energy spectrum evolves to a stationary state that is independent of initial conditions.

For all the flows considered in this study, the stationary energy spectrum that emerges satisfies an approximate power law, with slope -1, for frequencies between f and N. In the ray-tracing equations we simulate there is no wave–wave interaction, nor feedback from wave packets to the background flow, thus the observed stationary spectrum must result from refraction by the background flow. Moreover, the spectrum of wave frequencies matches that predicted by tracking the exponentially growing eigenvectors of the flow field, consistent with wave capture theory (Bühler and McIntyre 2005). Remarkably, this holds for both steady and unsteady background flows. The success with unsteady flows suggests a connection to the stochastic trajectory model of HA97; following the same idea here, a theoretical frequency spectrum derived in section 6 matches our simulated results with remarkable accuracy, even predicting an energy maximum that occurs for large Burger number.

One caveat of this study is that it is based on the WKB approximation, which formally requires that the length scale of wave packets be much smaller than that of the background flow. This might seem to limit the relevance of our findings to the refraction of wind-generated near-inertial oscillations (NIO) by the mesoscale eddy field, whose lateral scales are the reverse of what is assumed by WKB. A similar concern applies to Kunze (1985), who used WKB to argue that the geostrophic flow with vorticity ζ should induce an effective frequency shift from f to $f + \zeta/2$.

Young and Jelloul (1997) revisited the problem using a multiscale asymptotic analysis approach that is independent of lateral scale. Their NIO equation for the wave amplitude demonstrates that NIOs can disperse vertically into the oceanic interior in a matter of days, consistent with observations. In the Young and Jelloul (1997) picture, the slowly varying background eddy flow acts as an inhomogeneous medium that refractively distorts the waves. Correlations develop between the wave amplitude and the eddy streamfunction, resulting in the emergence of a lateral wave scale similar to the eddy scale, along with a concomitant frequency shift and increased downward propagation rate. Their theory, however, is unable to predict the dramatic spread in frequencies found in the present study, as their underlying asymptotic approach is limited to frequencies near f.

Nevertheless, picking up the wave evolution problem where the picture above ends, a WKB approach to the wave field becomes easier to rationalize. Taking this point of view, our findings suggest that NIO energy, once distorted by the eddy field, is then further refracted, filling out a continuum of wave energy. While the emergent wave energy frequency spectrum is remarkably robust, we caution against making a too-direct comparison between our results and the GM spectrum:

1) While a universal spectrum emerges from our study, the simulations that produce it are freely evolving. Frequencies are bound to lie between f and N, but no such bound exists on the wavenumbers. In real flows, wave energy will be injected at some rate, and high wavenumber waves will break and dissipate, presumably forming a steady state—but this steady state need not be associated with the energy spectrum found for the freely evolving case studied here.
2) It is important to note that the energy spectrum found here is a function of the *intrinsic* frequency, i.e., the frequency observed in a Lagrangian frame following wave packets. By contrast, the GM spectrum was developed to model the wave spectrum measured in the Eulerian frame. For example, the "moored spectrum" (e.g., Garrett and Munk 1975) provides the energy spectrum as a function of frequency and depth, relevant to time series collected from a moored current meter. This spectrum falls off like ω_a^{-2}. In the steady-flow cases, the absolute frequency is conserved, making the difference between measuring one versus the other quite stark! The fact that the same spectrum emerges when the flow is unsteady, however, also suggests that conservation of absolute frequency is not a prerequisite for our results.

We leave further investigation of the connection between our results and the oceanic internal wavefield to future research.

Acknowledgments. The authors thank Eric Kunze for interesting and useful comments on this work. KSS acknowledges support from NASA Award 80NSSC20K1142, and OB acknowledges support from ONR Grant N00014-19-1-2407 and NSF Grant DMS-2108225. All authors thank three anonymous reviewers for useful comments that have improved the paper.

Data availability statement. The numerical models for all the simulations presented here can be downloaded from https://github.com/WenjingDong/raytracing3DforJPO.

APPENDIX

Numerical Details

Here we describe the numerical methods for solving the ray tracing equations (1). For each wave packet, the velocity and velocity gradient at $\mathbf{x}(t)$ are evaluated exactly at each time step. For the synthetic Charney turbulent flows, we evaluate the velocity and velocity gradient by using the three-dimensional Fourier components of the streamfunction directly. For example, the velocity in a steady Charney turbulent flow specified by (7) is

$$(U, V)(\mathbf{x}) = C \sum_{\mathbf{q}_s : Q_1 < q_s < Q_2} \times i(-q_y, q_x)\exp[i(q_x x + q_y y + q_z z + \theta)]q_s^{-7/2}. \tag{A1}$$

Velocity and velocity gradients can be evaluated similarly in unsteady Charney turbulent flows since the flows are periodic in three dimensions.

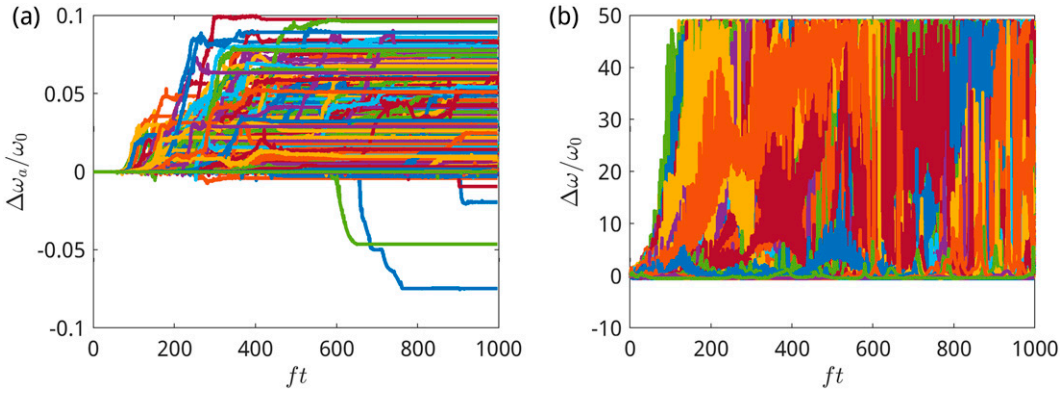

FIG. A1. (a) Evolution of the relative error of the absolute frequency and (b) evolution of the relative intrinsic frequency change in the QG flow.

For the simulated QG flow, which is horizontally periodic but vertically bounded, we make even extension of the streamfunction in a domain of height $2H$, i.e.,

$$\psi_{\text{ext}}(x, y, z) = \begin{cases} \psi(x, y, z), & z > 0, \\ \psi(x, y, -z), & z < 0. \end{cases} \tag{A2}$$

Then ψ_{ext} can be written as a Fourier series, i.e.,

$$\psi_{\text{ext}}(x, y, z) = \sum_{\mathbf{q}} \sum_{n=0}^{20} \frac{1}{2}[\delta_{q_z, n\pi/H} + \delta_{q_z, -n\pi/H}]\hat{\psi}_n(q_x, q_y)\exp[i(q_x x + q_y y + q_z z)], \tag{A3}$$

where $\delta_{q_z, n\pi/H}$ and $\delta_{q_z, -n\pi/H}$ are Kronecker deltas, and q_z is summed over the set $\{-40\pi/2H, -39\pi/2H, \ldots, 39\pi/2H, 40\pi/2H\}$. Velocity and velocity gradient at any location $\mathbf{x}$ can be evaluated using the Fourier series as evaluated for synthetic Charney turbulent flows.

The ray tracing equations are integrated in time using a second-order Runge–Kutta method. The time step $\Delta t = c \min\left\{L/\left(n_x\sqrt{c_x^2 + c_y^2}\right), H/(n_z|c_z|)\right\}$, where (c_x, c_y, c_z) is the initial group velocity and $c \ll 1$, is a constant determined to ensure that absolute frequency is conserved in the steady background flows. As Okubo–Weiss D can be positive, the second equation in (1) is numerically unstable. Therefore, c is much smaller than 1 and indeed $c = 0.02$ in the QG background flow. Figure A1 shows the relative error of absolute frequency in the QG background flow is less than 10%, while the intrinsic frequency changes significantly.

REFERENCES

Alford, M. H., J. A. MacKinnon, H. L. Simmons, and J. D. Nash, 2016: Near-inertial internal gravity waves in the ocean. *Annu. Rev. Mar. Sci.*, **8**, 95–123, https://doi.org/10.1146/annurev-marine-010814-015746.

Armi, L., and P. Flament, 1985: Cautionary remarks on the spectral interpretation of turbulent flows. *J. Geophys. Res.*, **90**, 11 779–11 782, https://doi.org/10.1029/JC090iC06p11779.

Barkan, R., K. B. Winters, and J. C. McWilliams, 2017: Stimulated imbalance and the enhancement of eddy kinetic energy dissipation by internal waves. *J. Phys. Oceanogr.*, **47**, 181–198, https://doi.org/10.1175/JPO-D-16-0117.1.

Bühler, O., and M. E. McIntyre, 2005: Wave capture and wave–vortex duality. *J. Fluid Mech.*, **534**, 67–95, https://doi.org/10.1017/S0022112005004374.

Charney, J. G., 1971: Geostrophic turbulence. *J. Atmos. Sci.*, **28**, 1087–1095, https://doi.org/10.1175/1520-0469(1971)028<1087:GT>2.0.CO;2.

Dong, W., O. Bühler, and K. S. Smith, 2020: Frequency diffusion of waves by unsteady flows. *J. Fluid Mech.*, **905**, R3, https://doi.org/10.1017/jfm.2020.837.

Garrett, C., and W. Munk, 1972: Space-time scales of internal waves. *Geophys. Fluid Dyn.*, **3**, 225–264, https://doi.org/10.1080/03091927208236082.

——, and ——, 1975: Space-time scales of internal waves: A progress report. *J. Geophys. Res.*, **80**, 291–297, https://doi.org/10.1029/JC080i003p00291.

Haynes, P., and J. Anglade, 1997: The vertical-scale cascade in atmospheric tracers due to large-scale differential advection. *J. Atmos. Sci.*, **54**, 1121–1136, https://doi.org/10.1175/1520-0469(1997)054<1121:TVSCIA>2.0.CO;2.

Kafiabad, H. A., M. A. Savva, and J. Vanneste, 2019: Diffusion of inertia-gravity waves by geostrophic turbulence. *J. Fluid Mech.*, **869**, R7, https://doi.org/10.1017/jfm.2019.300.

Kunze, E., 1985: Near-inertial wave propagation in geostrophic shear. *J. Phys. Oceanogr.*, **15**, 544–565, https://doi.org/10.1175/1520-0485(1985)015<0544:NIWPIG>2.0.CO;2.

Lelong, M.-P., and J. J. Riley, 1991: Internal wave—Vortical mode interactions in strongly stratified flows. *J. Fluid Mech.*, **232**, 1–19, https://doi.org/10.1017/S0022112091003609.

MacKinnon, J. A., and Coauthors, 2017: Climate process team on internal wave–driven ocean mixing. *Bull. Amer. Meteor. Soc.*, **98**, 2429–2454, https://doi.org/10.1175/BAMS-D-16-0030.1.

McComas, C. H., and F. P. Bretherton, 1977: Resonant interaction of oceanic internal waves. *J. Geophys. Res.*, **82**, 1397–1412, https://doi.org/10.1029/JC082i009p01397.

Polzin, K. L., and Y. V. Lvov, 2011: Toward regional characterizations of the oceanic internal wavefield. *Rev. Geophys.*, **49**, RG4003, https://doi.org/10.1029/2010RG000329.

Rocha, C. B., G. L. Wagner, and W. R. Young, 2018: Stimulated generation: Extraction of energy from balanced flow by near-

inertial waves. *J. Fluid Mech.*, **847**, 417–451, https://doi.org/10.1017/jfm.2018.308.

Savva, M. A., and J. Vanneste, 2018: Scattering of internal tides by barotropic quasigeostrophic flows. *J. Fluid Mech.*, **856**, 504–530, https://doi.org/10.1017/jfm.2018.694.

——, H. A. Kafiabad, and J. Vanneste, 2021: Inertia-gravity-wave scattering by three-dimensional geostrophic turbulence. *J. Fluid Mech.*, **916**, A6, https://doi.org/10.1017/jfm.2021.205.

Shakespeare, C. J., and J. Taylor, 2014: The spontaneous generation of inertia–gravity waves during frontogenesis forced by large strain: Theory. *J. Fluid Mech.*, **757**, 817–853, https://doi.org/10.1017/jfm.2014.514.

Sugiyama, Y., Y. Niwa, and T. Hibiya, 2009: Numerically reproduced internal wave spectra in the deep ocean. *Geophys. Res. Lett.*, **36**, L07601, https://doi.org/10.1029/2008GL036825.

Thomas, J., and S. Arun, 2020: Near-inertial waves and geostrophic turbulence. *Phys. Rev. Fluids*, **5**, 014801, https://doi.org/10.1103/PhysRevFluids.5.014801.

Thomas, L. N., 2012: On the effects of frontogenetic strain on symmetric instability and inertia–gravity waves. *J. Fluid Mech.*, **711**, 620–640, https://doi.org/10.1017/jfm.2012.416.

Ward, M. L., and W. K. Dewar, 2010: Scattering of gravity waves by potential vorticity in a shallow-water fluid. *J. Fluid Mech.*, **663**, 478–506, https://doi.org/10.1017/S0022112010003721.

Whalen, C. B., C. De Lavergne, A. C. Naveira Garabato, J. M. Klymak, J. A. Mackinnon, and K. L. Sheen, 2020: Internal wave-driven mixing: Governing processes and consequences for climate. *Nat. Rev. Earth Environ.*, **1**, 606–621, https://doi.org/10.1038/s43017-020-0097-z.

Young, W., and M. B. Jelloul, 1997: Propagation of near-inertial oscillations through a geostrophic flow. *J. Mar. Res.*, **55**, 735–766, https://doi.org/10.1357/0022240973224283.